Colloids and Surfaces B: Biointerfaces 189 (2020) 110842

Contents lists available at ScienceDirect

Colloids and Surfaces B: Biointerfaces

journal homepage: www.elsevier.com/locate/colsurfb

Bioinspired red blood cell membrane-encapsulated biomimetic nanoconstructs for synergistic and efficacious chemo-photothermal therapy

Pei Wang[a,1], Fuquan Jiang[b,1], Biaoqi Chen[c], Hanxiao Tang[c], Xiaojiao Zeng[a], Duanhua Cai[c], Mingzhi Zhu[c], Ruimin Long[c], Dayun Yang[e], Ranjith Kumar Kankala[c,d], Shibin Wang[a,d], Yuangang Liu[c,d,f,*]

[a] College of Materials Science and Engineering, Huaqiao University, Xiamen, Fujian 361021, PR China
[b] School of Pharmaceutical Sciences, Fujian Provincial Key Laboratory of Innovative Drug Target Research, Xiamen University, Xiamen, Fujian, 361021, PR China
[c] College of Chemical Engineering, Huaqiao University, Xiamen, Fujian, 361021, PR China
[d] Fujian Provincial Key Laboratory of Biochemical Technology, Xiamen, Fujian, 361021, PR China
[e] School of Basic Medical Science, Fujian Medical University, Fuzhou, Fujian, 350122, PR China
[f] Institute of Pharmaceutical Engineering, Huaqiao University, Xiamen, Fujian, 361021, PR China

ARTICLE INFO

Keywords:
Biomimetic nanoparticles
Gambogic acid
Bovine serum albumin
Red blood cell membrane
Chemo-photothermal therapy

ABSTRACT

Recently, the fabrication of nanotechnology-based co-delivery systems has garnered enormous interest for efficacious cancer therapy. However, these systems still face certain challenges such as codelivery of drugs with different chemistries, inadequate loading efficiency, immune rejection resulting in rapid clearance and substantially poor bioavailability *in vivo*. To address the challenges, we have developed a biomimetic and stable design based on bovine serum albumin (BSA) nanoparticles that are encapsulated with a hydrophilic photothermal agent, indocyanine green (ICG), as well as a hydrophobic agent, gambogic acid (GA), *via* the desolvation method. Furthermore, these nanoconstructs have been coated with the red blood cell membranes (RBCm), which exhibit pronounced long-term circulation in addition to avoiding premature leakage of drugs. RBCm-coated BSA nanoparticles show a higher affinity towards both GA and ICG (RmGIB NPs), resulting in high loading efficiencies of 24.3 ± 1.2 % and 25.0 ± 1.2 %, respectively. Moreover, the bio-efficacy investigations of these biomimetic constructs (RmGIB NPs) in cells *in vitro* as well as in tumor-bearing mice *in vivo* confirm augmented inhibition, demonstrating potential synergistic chemo-photothermal therapeutic efficacy. Altogether, we provide an efficient delivery platform for designing and constructing BSA nanovehicles toward synergistic and effective co-delivery of therapeutics.

1. Introduction

Among various traditional therapeutic modes available, chemotherapy using effective drugs has attracted significant attention from researchers as one of the most promising alternatives for treating a wide range of tumors [1]. In spite of progress over the decades in improving the bioavailability of drugs and other innovative strategies, current research on nanomedicine has shifted its focus toward combinatorial therapy, either by using a co-delivery approach that deliver multiple agents or by applying external stimuli such as light, ultrasound or a magnetic field for exhibiting synergistic therapeutic efficiency through different mechanisms [2,3]. In this framework, photothermal therapy (PTT), a non-invasive approach, is one of the advanced therapeutic strategies often applied for localized tumor ablation mediated by photosensitizers, which could offer minimal damage to the adjacent normal tissues [4,5]. However, utilization of PTT alone has no significant tumor ablating effects due to issues related to the inadequate penetration depth of light, resulting in the development of thermoresistance and substantial uncontrolled malignancy in various visceral organs [6,7]. These consequences necessarily demand breakthroughs to achieve better therapeutic effects. In an attempt to address this need, we hypothesize that integrating multiple therapeutic strategies, for instance, chemo-photothermal therapy, could offer synergistic tumor inhibition effects while concomitantly minimizing the side effects associated with chemotherapeutic agents and overcoming the problems related to light-based therapy [8,9].

* Corresponding author at: College of Chemical Engineering, Huaqiao University, Xiamen, Fujian, 361021, PR China.
E-mail address: ygliu@hqu.edu.cn (Y. Liu).
[1] These authors contributed equally to this work.

https://doi.org/10.1016/j.colsurfb.2020.110842
Received 4 October 2019; Received in revised form 30 January 2020; Accepted 1 February 2020
Available online 03 February 2020
0927-7765/

Indocyanine green (ICG) is one of the near infrared (NIR) dyes approved United States Food and Drug Administration (FDA), which acts on ablating tumors by not only transforming the absorbed light energy to heat *via* PTT but also by generating deadly singlet oxygen *via* photodynamic therapy (PDT). To address the poor stability issues and augment tumor specificity, several carrier systems have been fabricated to encapsulate ICG for diverse biomedical applications, such as polyallylamine, calcium phosphosilicate, lipid-polymer, and perfluorocarbon [10]. Besides, gambogic acid (GA) extracted from the Garcinia hanburryi tree has been demonstrated to be a potent natural and wide anticancer product and an inhibitor of 90-kDa heat shock protein (Hsp90), a key protein for inducing thermoresistance in the hypothermic cell during PTT [5]. However, the clinical application of GA limited by its poor water solubility ($<5\ \mu g\ mL^{-1}$) and short half-life (<4 h) [11,12], therefore it is critical to improve solubility and prolong the circulation of GA when combining chemotherapy with PTT.

More often, the fabrication of various nanoparticles-based drug delivery carriers suffers from a significant limitation of low drug loading efficiency because in most cases, the affinity between the guest molecules and host is managed by weak interactions such as physical adsorption through hydrogen bonding, electrostatic interactions, hydrophobic interactions or chemical crosslinking, which subsequently also results in premature leakage, significantly affecting the therapeutic dosage regimen in cancer therapy [13]. On the contrary, self-assembled drug nanoconstructs could be an alternative to overcome the limitation of poor delivery efficiency as well as loading ability. However, these constructs also face the shortcomings of poor stability and failing to achieve long-term circulation due to rapid clearance in the blood. To address these limitations, it is convenient to utilize biomolecules such as proteins as carriers owing to their amphipath and three-dimensional (3D) architectures. Bovine serum albumin (BSA) is one such biomolecule that has garnered enormous interest from researchers for use in drug delivery systems due to its advantageous features: cost-effectiveness, ease of preparation and purification, as well as unusual ligand-binding properties [14]. Paclitaxel-albumin nanoparticle (nab-paclitaxel, Abraxane®) is one such protein-based formulation marketed to delivery paclitaxel [15], but nanomedicine has been facing a significant obstacle in promoting the clinical formulations due to their heterogeneity in elimination by the reticuloendothelial system (RES), resulting in impaired long-term circulation and subsequently reduced in their passive accumulation in tumor tissue [16–19]. In an attempt to address this issue, several advancements have been made such as surface modification to combat recognition *via* various approaches, and diverse morphologies based on particle size, shape, and flexibility, among others [20–23]. In this framework, biomimetic drug carriers have been reported for extending circulation time by using, for example, red blood cells (RBCs) as carriers to deliver enzymes and drugs. Zhang and colleagues firstly reported stable red blood cell membrane (RBCm)-camouflaged polymeric nanoparticles with a longer elimination half-life over conventional polyethylene glycol (PEG)-coated nanoparticles. These constructs possessed antigenic and immunogenic properties as potential haptenes, owing to their intrinsic properties (membrane protein, CD47) [24–26]. Since then, numerous efforts have been made in the research of RBCm and other cell membranes for fabricating biomimetic drug delivery system [27–30].

Inspired by these facts, herein, we fabricated innovative RBCm-coated BSA nanoconstructs encapsulated with GA (hydrophobic drug) and ICG (hydrophilic agent) for achieving long-term circulation in the blood to be used in synergistic chemo-/photothermal therapy. Initially, GA and ICG were encapsulated in the BSA network (GIB nanoconstructs) using the solvent displacement method and further coated with the RBCm, which was extracted from the blood of Balb/c nude mice (Fig. 1) [31]. Moreover, on the basis of the simplicity of this assembly, with intentionally selected hydrophobic/hydrophilic agents and different kinds of protein, the bioinspired strategy could offer various ways for the design of clinically translatable nanocarriers to achieve a highly efficient therapy for diverse diseases.

2. Experimental section

2.1. Materials

ICG was obtained from Sangon Biotech Co. Ltd. (Shanghai, China), GA from Desite Biological Co. Ltd. (Chengdu, China), BSA from Aladdin Biochemical Technology Co. Ltd. (Shanghai, China) and glutaraldehydefrom Xilong Scientific Co. Ltd. (Guangzhou, China). Dulbecco's Modified Eagle Medium (DMEM), fetal bovine serum (FBS), penicillin, and streptomycin were purchased from Biological Industries Ltd. (Hertzliya Pituach, Israel). Mammary epithelial basal medium (MEBM) and the additives were obtained from Lonza/Clonetics Corporation (Basel, Switzerland). MCF-10A cells (human breast epithelial cell line), MDA-MB-231 cells (human breast adenocarcinoma cell line), MCF-7 cells (human breast adenocarcinoma cell line), HeLa cells (human cervical cancer cells) and L929 cells (mouse fibroblast cell line) were obtained from the Type Culture Collection of the Chinese Academy of Sciences (CAS, Shanghai, China). MTT Cell Proliferation and Cytotoxicity Assay Kit and Calcein-AM/PI Double Stain Kit were purchased from KeyGene Biotech (Nanjing, China). 4′,6-Diamidino-2-phenylindole (DAPI) staining solution was acquired from Solarbio Co. Ltd. (Beijing, China) and 1,1′-dioctadecyl-3,3,3′,3′-tetramethylindocarbocyanine perchlorate (DiI, $\lambda_{Ex/Em}$ = 549/565 nm) was acquired from Beyotime Biotechnology Co. Ltd. (Shanghai, China).

2.2. Preparation of GIB NPs

The GIB NPs were prepared using a solvent displacement approach [15]. Briefly, the GA and ICG were initially dissolved in methanol (1 mL) at different concentrations. The mixture was added dropwise to BSA in phosphate-buffered saline (PBS, pH-7.4) with vigorous stirring and then glutaraldehyde was added and stirred at room temperature for 24 h. Finally, the resultant GIB NPs were collected and washed several times using deionized water.

2.3. Extraction of RBCm-derived vesicles

The whole blood from mice (6–8 weeks, Huafukang Biotechnology Co. Ltd., Beijing, China) was first collected in a heparin-coated blood collection tube through retroorbital sinus puncture and then the blood was centrifuged at 1000 rpm for 5 min at 4 °C for separating plasma. The resultant RBCs were washed with PBS three times and then suspended in deionized water at 4 °C for 60 min. The hemoglobin was removed after centrifuging at 10,000 rpm for 5 min, and then the RBCm was washed with deionized water several times. The collected RBC ghosts were sonicated using a bath sonicator KQ5200DE, Kun Shan Ultrasonic Instruments Co. Ltd. for 5 min at 40 kHz frequency and 200 W power [31]. Furthermore, the size of the RBCm-derived vesicles was measured by dynamic light scattering (DLS; NanoBrook Omni, Brookhaven Instruments Co. Ltd.). Briefly, the RBCm was stained with DiI ($\lambda_{Ex/Em}$ = 549/565 nm) to monitor the RBCm-coated NPs in the subsequent process.

2.4. Preparation of RBCm-cloaked NPs

RmGIB NPs were fabricated by dispersing and fusing RBCm vesicles with GIB NPs in the appropriate ratio using bath sonicator at a frequency of 40 kHz and a power of 200 W for 3 min. To conduct RBCm cloaking, RBCm labeled with DiI in the previous step was used. Due to specific interactions between the fluorescent probe and membrane-bonded protein, a red fluorescence was emitted and could be detected by confocal laser scanning microscopy (CLSM; 100× oil objective lens, Leica TCS SP8, Wetzlar, Germany). Subsequently, the amount of RBCm-coated GIB NPs was quantified by flow cytometry (Moflo-XDP,

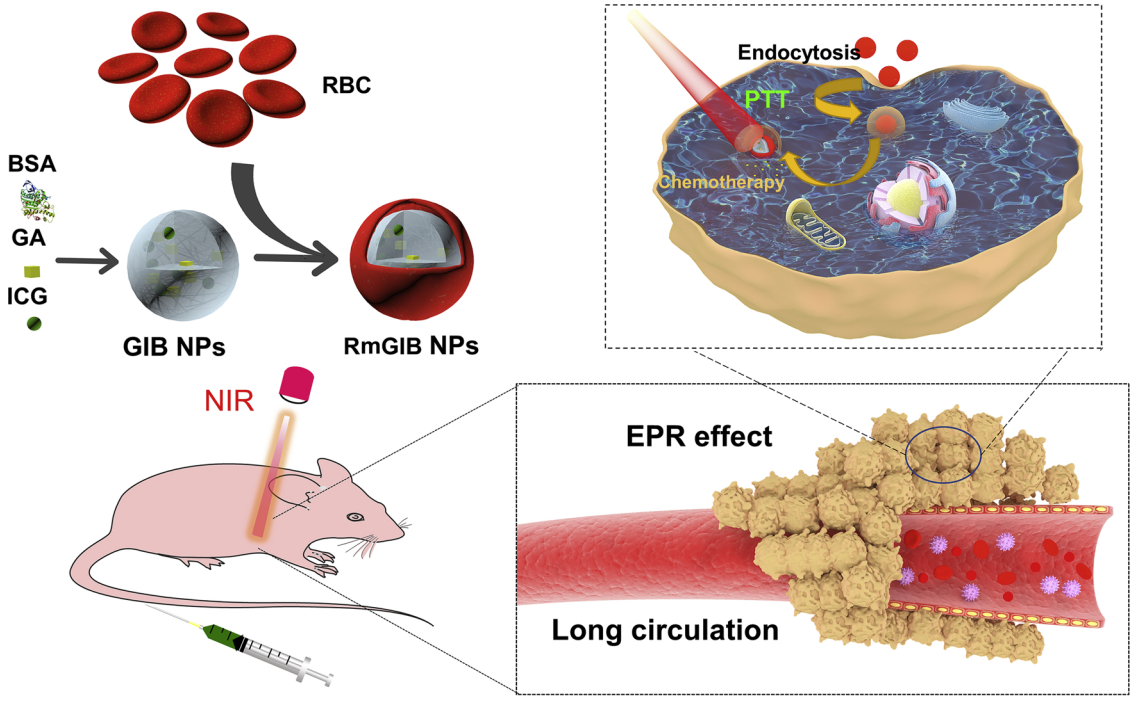

Fig. 1. Schematic of the preparation process for RBCm-coated BSA nanoparicles showing higher affinity towards both GA and ICG (RmGIB NPs) to be used in a synergistic chemo-therapy for cancer.

Beckmancoulter). RmGIB NPs were dissolved in DMSO solution, and the concentration of GA and ICG were then determined by using UV–vis spectroscopy at a maximum wavelength of 360 nm and 780 nm, respectively, correlating to their corresponding pre-recorded calibration curve. The loading capacity (LC) of GA and ICG was calculated by the following formula:

$$LC\ (\%) = M_D/(M_N + M_D) \times 100 \quad (1)$$

where M_D is the loading weight of drug (GA or ICG) and M_N is the loading weight of RmGIB NPs.

2.5. Physical characterizations

The loading efficiency and the confirmation of the appropriate ratios for the different drugs were confirmed by scanning the GIB NPs using UV–vis-NIR spectroscopy. The particle diameter and distribution, as well as the surface zeta potential of GIB NPs and RmGIB NPs (n = 3), were obtained by DLS measurements. Fourier transform infrared spectroscopy (FTIR; Thermo Scientific Nicolet iS 50) was used to analyze the characteristic chemical functionalities of the prepared GIB NPs and RBCm-coated nanocomposites. Morphological attributes were determined by transmission electron microscopy (TEM; Hitachi S-4800, Tokyo Japan). The samples for TEM observations were prepared by depositing them on 300-mesh copper grids at 100 kV after negative staining by phosphotungstic acid for 1 min and then air-drying the slides for 12 h.

2.6. In vitro release of drugs

To study the release efficiencies of both drugs, GIB NPs and RmGIB NPs were placed separately in a dialysis bag and suspended in the buffer (20 mL, 10 mM, pH 7.4) containing 1 % Tween-80. Furthermore, the samples containing buffer were placed in a horizontal shaker maintained at 37 °C and stirred at 100 rpm. A 2-mL aliquot of dispersion solution was collected at the desired time points and a fresh equivalent volume of PBS was replenished. The released amounts of GA and ICG in the solution were measured by correlating their corresponding absorbance values obtained using UV–vis-NIR spectrometry. All the tests and measurements were carried out in triplicate.

2.7. NIR-induced photothermal efficacy in vitro

An aqueous dispersion of GIB NPs (1 mL, 0.1 mg mL^{-1}) or RmGIB NPs (with GIB NPs concentration equivalent to 0.1 mg mL^{-1}) placed in a transparent quartz vial (4 mL) was irradiated with a fiber-coupled continuous semiconductor diode laser (MDL-*N*-808 nm-10 W, New Industries Optoelectronics Technology Co., Ltd. Changchun, China) at a power density of 1.5 W cm^{-2} for 5 min. Furthermore, the temperature was monitored with a thermal infrared imaging camera (Tis65, USA). After repeating for five cycles, UV–vis-NIR absorbance spectra of the solution before and after irradiation were recorded.

2.8. Anticancer efficacy in vitro

HeLa cells were seeded in a 96-well plate at a density of 1×10^4 cells per well and cultured for 24 h at 37 °C. Furthermore, the treatments were continued by replacing the media with fresh media containing ICG (20 μg mL^{-1}), RmGB NPs (GA concentration equivalent to 20 μg mL^{-1}), RmGIB NPs (ICG concentration equivalent to 20 μg mL^{-1} and GA concentration to 20 μg mL^{-1}), respectively. After 2 h of incubation, the corresponding wells were irradiated with an 808 nm NIR laser (1.5 W cm^{-2}) for 3 min. The media were replaced with fresh media and then incubated for 18 h. Afterwards, the media were replaced with 100 μL of fresh medium and 10 μL MTT (0.5 mg mL^{-1}) and then continuously incubated for 4 h. Subsequently, 150 μL of DMSO was added into each well after removing the media. The relative cell viability was calculated according to the following equation:

$$\text{Cell viability}\ (\%) = (OD_{treated} - OD_{blank})/(OD_{control} - OD_{blank}) \times 100 \quad (2)$$

where $OD_{treated}$ is the absorbance of the group of microparticles, OD_{blank} is the absorbance of the group with no cells, and $OD_{control}$ is the control group.

A calcein-AM/PI assay was also employed to visually explore the

antitumor activity of RmGIB NPs *in vitro*. HeLa cells were seeded in the confocal dishes at a density of 2×10^4 cells per well with 2 mL of media and cultured for 24 h at 37 °C. HeLa cells were stained with calcein-AM/PI stain after being treated with nanoparticles and NIR irradiation and then observed using CLSM.

2.9. Cellular uptake of GIB NPs and RmGIB NPs

HeLa cells and MCF-7 cells were seeded at a density of 2×10^5 per mL on a 24-well plate. The media were replaced with free media containing GB NPs and GIB NPs after incubating overnight. The media were then removed and the cells were washed twice using PBS for removing the residual nanoparticles after incubating several hours. The cells growing on the dish glasses were stained with DAPI, put on the microscope slides and observed using CLSM.

2.10. In vivo chemo-photothermal efficacy

All experimental protocols utilizing animals were performed according to the Experimental Animal Ethics Committee of Fujian Medical University following the guidelines of the National Institute of Health Animal Care and the Animal Management Rules of the Ministry of Health of the People's Republic of China. Nude mice (female, 6 weeks old) bearing subcutaneous HeLa tumors (approx. 100 mm^3 in volume) were randomly divided into five groups: (1) 200 μL of PBS with NIR laser irradiation at the power density of 1.5 W cm^{-2} for 5 min; (2) 200 μL of free GB (1 mg mL^{-1}); (3) 200 μL of free ICG (1 mg mL^{-1}) with NIR laser irradiation (1.5 W cm^{-2}, 5 min); (4) 200 μL of RmGIB NPs, (5) 200 μL of RmGIB NPs with NIR laser irradiation (1.5 W cm^{-2}, 5 min). All the nanoparticles were injected intravenously into the mice *via* the tail vein. The mouse body weight and the volume of the tumor were measured every day and calculated as tumor volume = (tumor length) × (tumor width)^2/2. The relative tumor volume (RTV) rate was calculated according to the following equation:

$$RTV\ (\%) = V_T/V_0 \times 100 \quad (3)$$

where V_T is the tumor volume after treatment and V_0 is the tumor volume before treatment. Thermal imaging was recorded by an infrared thermal imaging camera (Tis65, Fluke, USA) before and after irradiation.

2.11. In vivo imaging and biodistribution of nanocomposites

After the tumor reached 100 mm^3 in volume, 200-μL samples of free ICG, GIB NPs and RmGIB NPs (in terms of ICG 1 mg mL^{-1}) were intravenously injected into mice and fluorescence images (filter set $\lambda_{Ex/Em}$ of ICG: 630/700 nm) were captured by a Carestream imaging system (Carestream FX Pro, Brookhaven Instruments Co. Ltd.). After 12 h, tumor-bearing mice were sacrificed by intraperitoneal injection with 4 % chloral hydrate and then dissected at the autopsy laboratory. The major organs (heart, liver, spleen, lung, and kidneys) and tumors were collected and the distribution of free ICG, GIB NPs, and RmGIB NPs *ex vivo* was determined. After completion of the experiment, the body, viscus and tumor tissue were collected for harmless treatment.

2.12. Statistical analysis

The statistical significance between two sets of data was calculated using Student's *t*-test. A p value of < 0.05 was considered to be statistically significant.

3. Results and discussion

3.1. Physicochemical characterizations

As shown in Fig. S1, the TEM observations indicated that the albumin-bound (nab™) technology resulted in uniform and discrete GB NPs of different sizes. Further, the hydrodynamic sizes (Fig. S2) were obtained from DLS measurements, with 0.2 %, 0.4 % and 0.8 % BSA as a surfactant providing physical stability in solution. The results showed that the ellipsoidal size of GB NPs in 0.2 % BSA was much bigger than the spherical size at 0.4 % and 0.8 % BSA, which indicated that the specific surface area of GB NPs diminished with a lack of BSA. However, the hydrodynamic sizes of GB NPs were bigger than from TEM observation, probably due to the interaction between surrounding water molecules and nanoparticles. The low polydispersity index (PDI) values of 0.22 ± 0.01, 0.19 ± 0.01 and 0.16 ± 0.03 for 0.2 %, 0.4 % and 0.8 % BSA, respectively, further supported the uniform size and good dispersibility of GB NPs in water. When the organic solution containing the hydrophobic drugs was dropped into the aqueous solution, the organic solution was dispersed into tiny droplets due to the shear force provided by high-speed rotation of the aqueous solution. Furthermore, BSA, as a surfactant, formed a film on the surface of the hydrophobic drugs to prevent contact between the drugs. When the concentration of BSA was low, it wasn't sufficient to prevent contact between the drugs, therefore the nanoparticle size was larger. Based on these results, 0.4 % BSA was chosen as the better condition for further studies. Furthermore, GIB NPs were prepared with different ratios of GA to ICG to determine the optimal proportion for combination therapy. Fig. 2A shows a decrease in the mean particle size of GIB NPs, proportional to the amount of GA, along with a reduction in the zeta potential, stabilizing at around -40 mV, indicates the stability of the constructs in aqueous solution [32,33]. Further, the UV–vis-NIR spectra of GIB NPs (Fig. 2B) at different ratios of GA to ICG showed that absorbance at 780 nm (the maximum absorption wavelength of ICG) increased with a larger amount of ICG, indicating the higher loading capacity of ICG. However, the particle size of GIB NPs was smaller compared to GB NPs at the respective conditions due to partial leakage of ICG from the aqueous phase, resulting in smaller droplets in the process of formation of GIB NPs. Based on these considerations, the optimal conditions for GIB NPs are a GA: ICG loading ratio of 1.04:1 and a mixing ratio of 8: 12, which were chosen in subsequent experiments.

Before extracting the RBCm *via* hemolytic treatment in a hypotonic solution, the cells were observed under a bright-field microscope. As shown in Fig. S3a, the images indicated that the RBCs kept their double-concave round cake shape. By contrast, the RBCm resulted in an indefinite shape after extraction from RBCs (Fig. S3b) and the mean size reduced from 2.67 ± 1.30 μm before sonication to 1.01 ± 0.08 μm after sonication, respectively (Fig. S4), which is better for cloaking unique nanoparticles. After coating with RBCm, TEM images of RmGIB NPs (Fig. 2F) depicted a characteristic core-shell structure, with a core and a uniform 10-nm thick outer membrane shell. To further confirm the RBCm coating over GIB NPs, the particle size and the surface zeta potential of NPs were measured before and after RBCm coating (Fig. 2D). Following membrane coating, the particle size of GIB NPs increased from 153.8 ± 4.9–180.3 ± 2.2 nm and the surface zeta potential changed from −41.3 ± 2.4 to −29.6 ± 0.7 mV, indicating that the RBCm was successfully coated over the nanoparticles *via* the established electrostatic interactions between GIB NPs and the phospholipid bilayer. This fluorescence colocalization of GIB NPs (red fluorescence) and RBCm stained with DiI (yellow fluorescence) further indicated an intact core-shell structure of the nanoparticles (Fig. S3). CLSM images (Fig. S5) and flow cytometric profiles of RmGIB NPs with DiI (Fig. S6) were measured to confirm the RBCm coating of GIB NPs. The above results further verify the successful coating of RBCm on the surface of GIB NPs. Furthermore, we determined the stability of RmGIB NPs in PBS and monitored the change of size and zeta potential by DLS

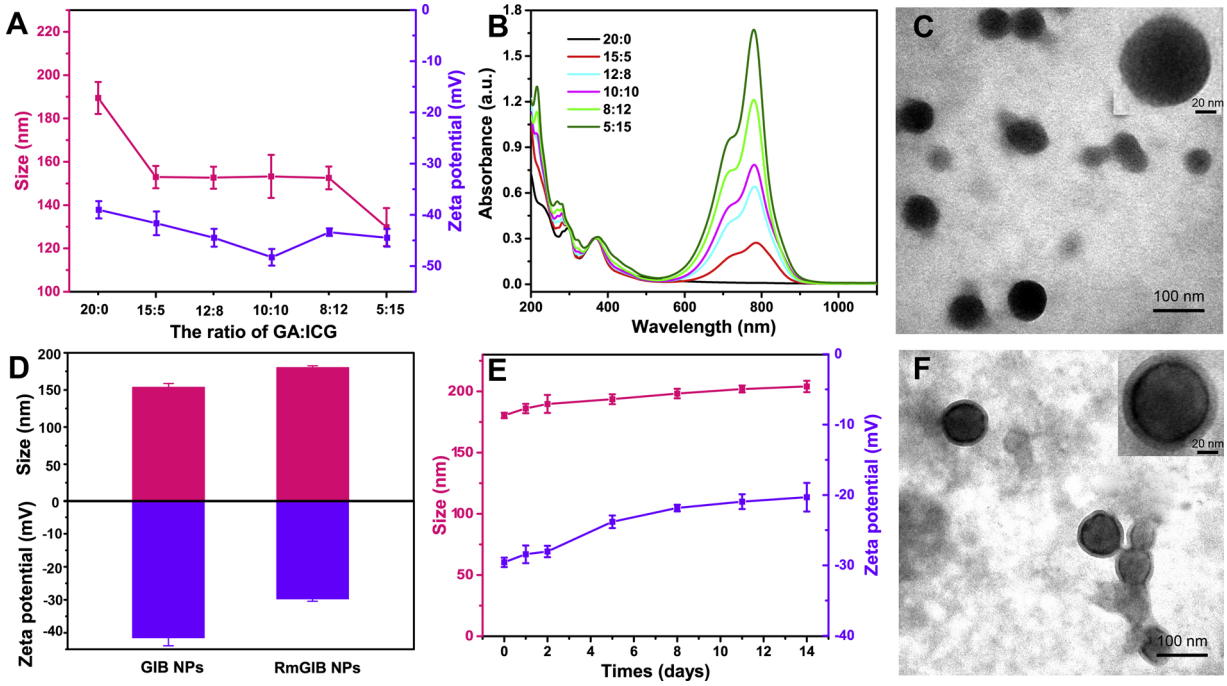

Fig. 2. (A) Mean particle size and zeta potential of GIB NPs with different mixing ratios of GA to ICG. (B) UV–vis-NIR spectra of GIB NPs from (A). (C) TEM images of GIB NPs in the ratio 8:12 (bar = 100 nm, 300k magnification in the inset). (D) Mean particle diameter and zeta potential of GIB NPs before (*left*) and following (*right*) RBCm coating. (E) DLS measurements of the size and surface zeta potential of RmGIB NPs over 14 days in PBS (pH 7.4). (F) TEM images of RmGIB NPs in the ratio 8:12. Data are expressed as the mean ± SD of three independent experiments.

(Fig. 2E). The average hydrodynamic diameter of RmGIB NPs increased from 180.3 ± 2.2–204.0 ± 4.7 nm, while, the zeta potential increased from −29.6 ± 0.7 to -20.3 ± 2.0 mV. The changes in size and zeta potential were likely caused by the fusion of a small number of excess RBCm vesicles in the particle solution [26].

3.2. In vitro photothermal properties of RmGIB NPs

UV-Vis-NIR spectra of various samples showed that the strong absorption of ICG in the nanoparticles and the subsequently coated sample at around 808 nm barely changed compared to free ICG (Fig. 3A), indicating that the preparation process for GIB NPs and RmGIB NPs has no significant influence on the stability of ICG. These results also provided evidence for RBCm coating of GIB NPs, where the absorption value of RmGIB NPs was higher than that of GIB NPs in the wavelength range 400 − 600 nm due to absorption of the phospholipid bilayer. Therefore, the high NIR absorbance coefficient and excellent photostability of RmGIB NPs would result in the substantial photothermal performance. Furthermore, the photothermal efficiency of ICG was determined by measuring the temperature of the samples after irradiation with light (power density: 1.5 W cm^{-2}). The results indicated that the temperature of RmGIB NPs increased in a concentration-dependent manner, indicating the efficiency of ICG in transforming light energy to heat energy (Fig. 3B). Interestingly, it was observed from the results that the temperature of the sample reached saturation at 39.5 °C for 50 μg mL^{-1} ICG and then reduced, which might be due to the rapid hydrolysis of ICG. However, the heat generated at that particular temperature still exchanged with the environment. Moreover, free ICG, GIB NPs, and RmGIB NPs presented similar temperature profiles, suggesting a negligible impact of the membrane coating (Fig. 3C). The temperature of RmGIB NPs increased rapidly to 54.8 °C for 100 μg mL^{-1} ICG during the NIR laser irradiation (power density: 1.5 W cm^{-2}) for 5 min, whereas the temperature of GB NPs and water increased by only about 1 °C.

3.3. In vitro GA loading and release from RmGIB NPs

The loading capacity of GA from GB NPs was measured as 79.0 ± 4.4 %, whereas that from GIB NPs decreased with decreasing ratio of GA to ICG due to the increasing content of hydrophilic ICG in the nanoparticles from Fig. 3B. Before the *in vitro* release study, the loading amounts of GA and ICG at ratio 8:12 in RmGIB NPs were determined as 24.3 ± 1.2 % and 25.0 ± , respectively. The high loading capacity can be ascribed to the following factors: (1) the solvent displacement method; (2) the electrostatic interaction between the positively charged part of BSA and the negatively charged ICG, as well as conjugation and hydrophobic interaction between BSA and the agents. The formation process of nanoparticles resulted in a colloidal system consisting of a hydrophobic core surrounded by hydrophilic BSA [15]. The reason why the total loading capacity of GA and ICG did not reach that of GB NPs, was the decreasing amount of GA and leakage of the hydrophilic agent ICG in PBS. The results (Fig. 3D, E, F) showed that the release of GA was sustained and slow in pH 7.4 PBS (simulating the physiological environment) and slower after RmGB NPs and RmGIB NPs, which confirmed the safety of RmGB NPs and RmGIB NPs in long-term blood circulation due to no drug leakage. Because GA and ICG need to pass through the phospholipid bilayer for release, there are hydrophobic interactions between them and the phospholipid.

3.4. In vitro antitumor performance

The toxicity and antitumor efficacy of free GA were evaluated using normal cells and tumor cells (Figs. S7, S9) for 24 h and 48 h, respectively. The results showed that GA exhibited great toxicity toward tumor cells and normal cells, even at a low concentration. The results showed that RmGIB NPs had lower toxicity toward normal cells than free GA at a low concentration range from 0.2 μg mL^{-1} to 1 μg mL^{-1} (Fig. S7). The results of the hemolysis test (Fig. S8) showed that RmGIB NPs had good biocompatibility at the concentration range from 1 μg mL^{-1} to 12 μg mL^{-1}, but there had hemolysis phenomenon due to the increasing concentration of GA released from RmGIB NPs when

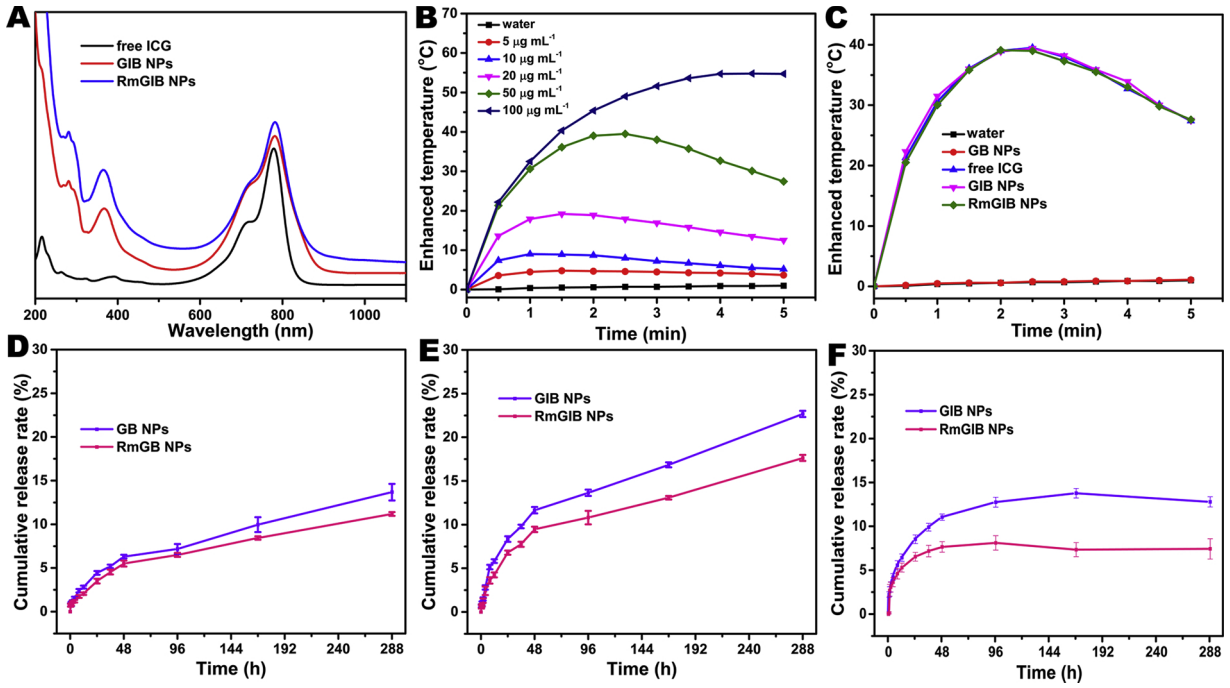

Fig. 3. (A) UV-Vis-NIR absorption spectra of GIB NPs and RmGIB NPs. (B) Temperature elevation of water and RmGIB NPs at different concentrations (5, 10, 20, 50, and 100 μg mL^{-1} in terms of ICG) irradiated by NIR laser (808 nm, 1.5 W cm^{-2}) for 5 min. (C) Temperature curves of water, GB NPs, free ICG, GIB NPs, and RmGIB NPs exposed to an 808 nm laser at a power density of 1.5 W cm^{-2} for 5 min. The concentration of ICG was the same for free ICG, GIB NPs and RmGIB NPs (50 μg mL^{-1} in terms of ICG). Cumulative release profiles of GA from (D) GB NPs and RmGB NPs and (E) GIB NPs and RmGIB NPs in PBS (pH 7.4). (F) Cumulative release profiles of ICG from GIB NPs and RmGIB NPs in PBS (pH 7.4). Data are expressed as the mean ± SD of three independent experiments.

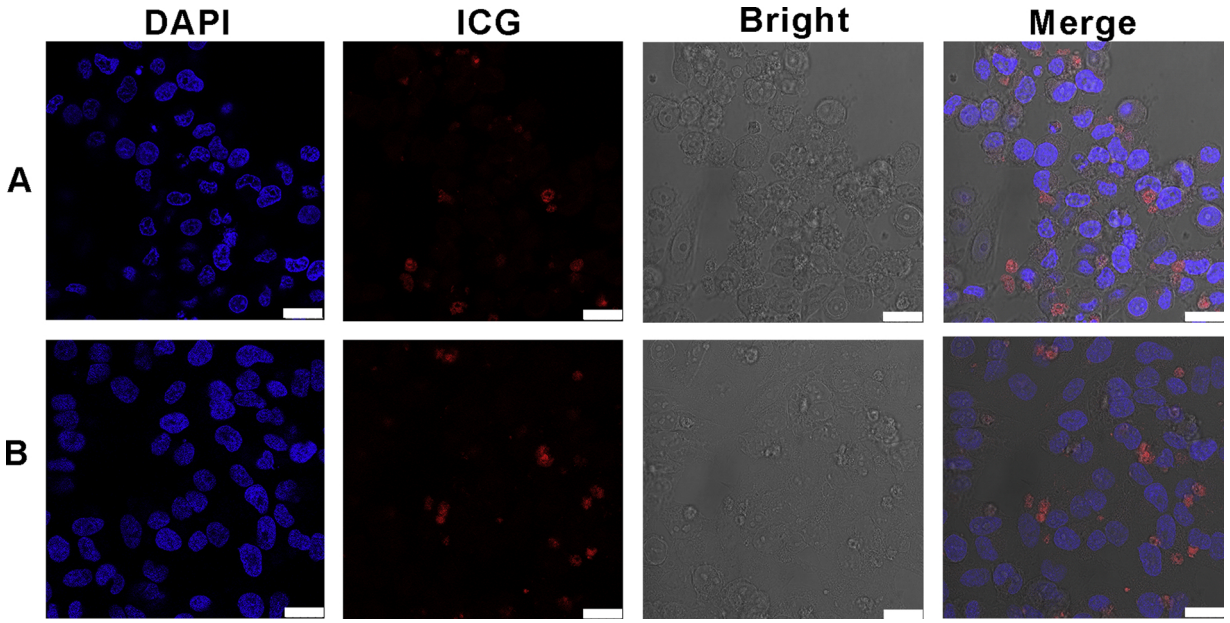

Fig. 4. Confocal laser scanning microscopy images of HeLa cells incubated with (A) GIB NPs and (B) RmGIB NPs for 3 h (bar = 25 μm).

concentration exceeded 12 μg mL^{-1}. In further investigations of the anti-tumor efficacy of GB NPs, GIB NPs, and RmGIB NPs, the results indicated that the samples substantially exhibited anti-tumor activity, indicating the efficacy of GA (Figs. S10, S11). To observe the cellular internalization of nanoparticles, both HeLa cells and MCF-7 cells were chosen as cell lines by staining the nucleus with DAPI (blue) against the red fluorescence of ICG from the sample. HeLa cells were cultured with GIB NPs and RmGIB NPs for 3 h and the results were obtained from CLSM after staining with DAPI. From Fig. 4, the red fluorescence of ICG was significantly observed inside and around the nuclei after endocytosis in 3 h. Furthermore, MCF-7 cells also endocytosed GIB NPs and RmGIB NPs in Fig. S12 after culturing for 3 h.

The *in vitro* chemo-photothermal anticancer activity of RmGIB NPs was detected by MTT assay and calcein-AM/propidium iodide (PI) (live/dead) staining. Neither GA nor laser irradiation had a significant anticancer effect against HeLa cells at high cell-seed density (Fig. 5A). The cell viability rates of RmGIB NPs were 68.99 ± 4.87 % and 12.27 ± 1.53 % without and NIR irradiation, respectively. Furthermore, the cell viability rate was 39.39 ± 5.46 % for photothermal therapy but there was no effect with chemotherapeutics. Under NIR

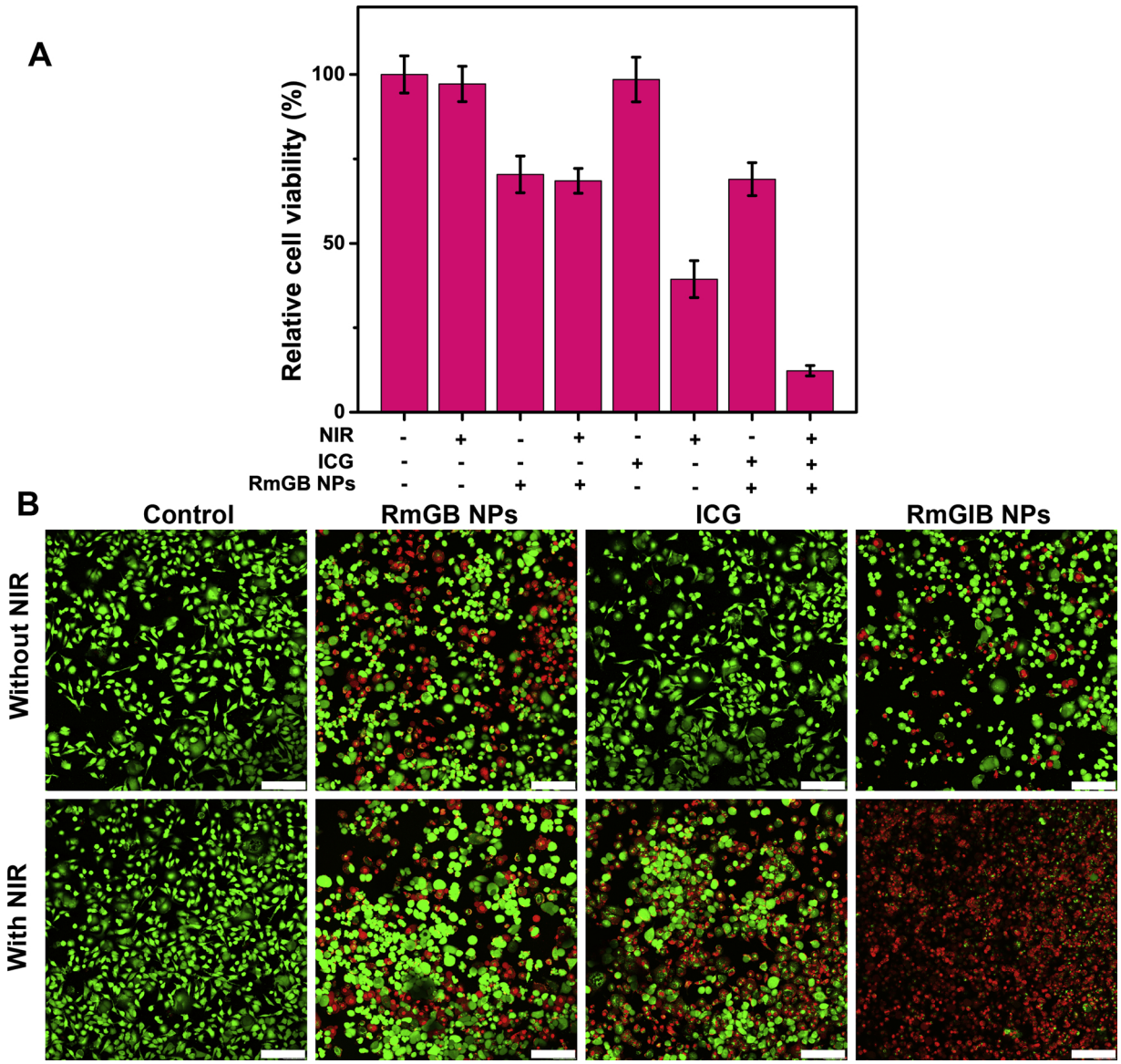

Fig. 5. (A) Cell viabilities of HeLa cells with different treatments. (B) Confocal laser scanning microscopy images of live/dead staining of HeLa cells cultured with different materials without or with NIR laser irradiation (808 nm, 1.5 W cm^{-2}) (scale bar = 200 μm). Data are presented as the mean ± SD ($n = 5$) and p-values are calculated using a two-sample Student's t-test, $^{***}P < 0.001$.

irradiation, most of the cells co-cultured with RmGIB NPs were stained with red fluorescence by PI (Fig. 5B), indicating that the live/dead staining corresponded to the MTT results. In addition, green fluorescence showed that the cells were alive in a control group, indicating that RmGIB NPs showed good anti-tumor effect and a significant combined therapeutic effect [34].

3.5. *In vivo* antitumor efficacy

Photothermal images (Fig. 6A) of mice intravenously injected with drugs or carriers confirmed that the temperature of RmGIB NPs increased higher than GIB NPs and free ICG because of the easy metabolism of free ICG *in vivo* after laser irradiation [35]. This was consistent with the experimental results in Fig. S13. The fluorescence images *ex vivo* showed that free ICG had almost no fluorescence in tumor tissue, which also indicates that ICG did not remain in tumor tissue. RmGIB NPs retained the most fluorescence in tumor tissue after 24 h, so the temperature increased to the highest temperature 44.5 °C under 808 nm NIR laser (1.5 W cm^{-2}) irradiation for 5 min. In addition, the local tumor temperature of mice injected with PBS, free ICG and GIB NPs increased to only 38.1 °C, 39.2 °C and 41.6 °C. The fluorescence intensity of RmGIB NPs in tumor tissue and kidney was stronger than that of GIB NPs, which indicated that the circulation time was longer *in vivo* after coating with the RBCm. It also indicated that RmGIB NPs had a potential application in photothermal therapy for tumors due to high heat-producing capacity and accumulation stemming from the long circulation of the RBCm. After laser irradiation, nude mice with cervical carcinomas were photographed to observe the size of tumor tissue over two weeks (Fig. 6B). In the previous few days, the tumor sizes changed slightly (Fig. 6C), indicating that the tumor was inhibited by chemotherapeutic drug GA or laser irradiation. However, compared with the poor anti-tumor efficiency of laser irradiation and free GA, RmGIB NPs with an RTV rate of around 86 % had significant efficacy in the tumor inhibited by the chemotherapeutic drug GA and laser irradiation, so there was no re-enlargement of tumor tissue within two weeks. Furthermore, RmGIB NPs had higher anti-tumor efficiency than the GA group with an RTV rate of around 10 % or the NIR irradiation group with an RTV rate of around 3 %, indicating that chemo-photothermal

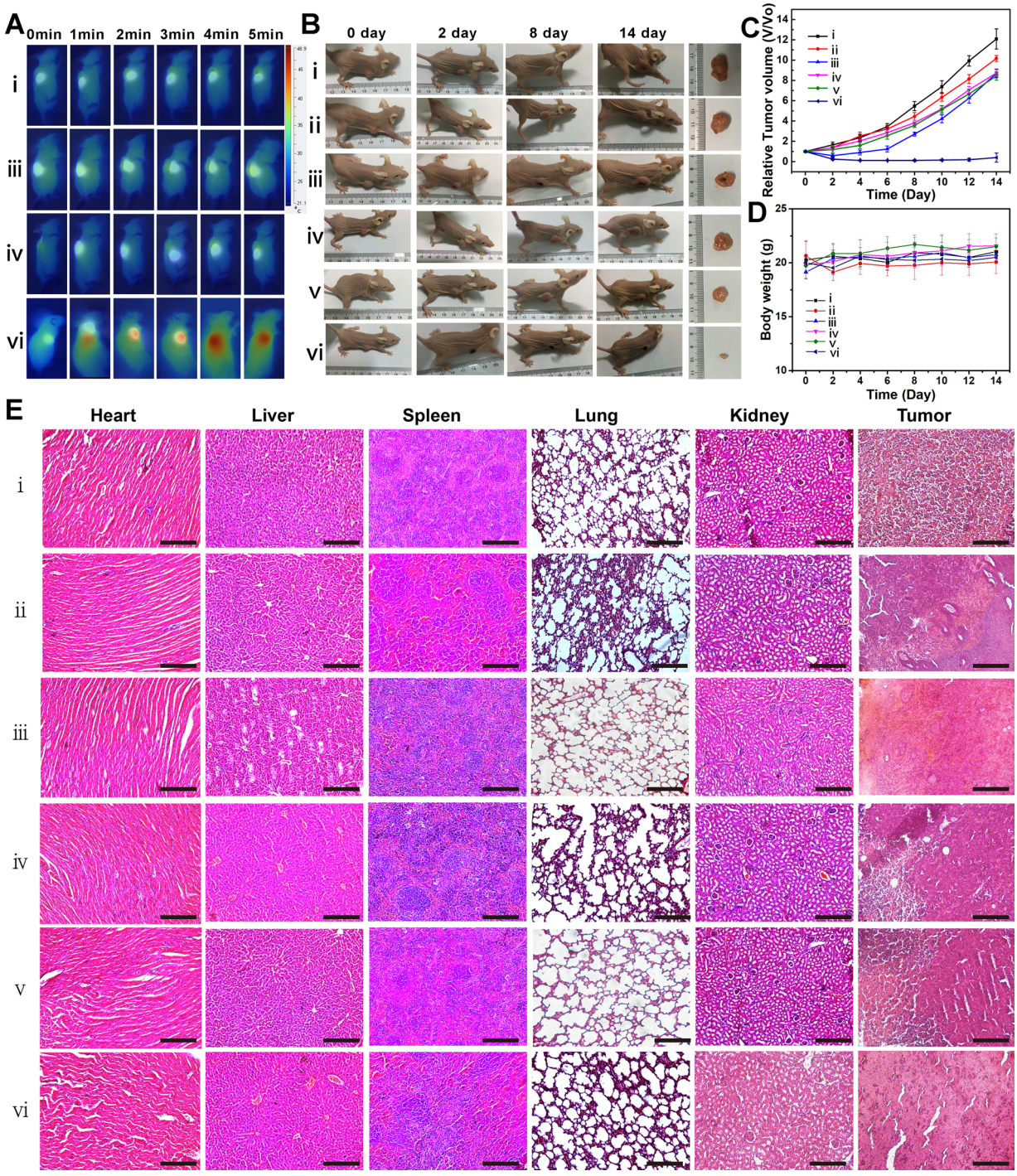

Fig. 6. (A) Infrared thermographic maps in the HeLa tumor-bearing nude mice irradiated by an 808 nm laser. *In vivo* anti-tumor effect of RmGIB NPs under irradiation, (B) photographs of HeLa tumor-bearing mice at different intervals after treatment with different formulations; (C) the calculated relative tumor size (V/V_0); and (D) the bodyweight of the tumor-bearing mice at various stages. (E) H&E staining of heart, spleen, lung, kidney, and tumor tissue slices for different treatment groups on Day 15: (i) PBS + NIR; (ii) free GA; (iii) free ICG + NIR; (iv) GIB NPs + NIR; (v) RmGIB NPs; (vi) RmGIB NPs + NIR. Scale bar = 100 μm. Data are expressed as the mean ± SD of five independent experiments.

combination therapy in the tumor was more effective than single therapy *in vivo*.

In the course of treatment, the weight of mice did not change significantly (Fig. 6D), indicating that the main organs were not damaged by the drug. To confirm this, H&E staining (Fig. 6E) of the main organs (heart, liver, spleen, lung, and kidney) was performed to observe that the cells of each organ were in good shape and not damaged, indicating good biocompatibility of the nanoparticles. Furthermore, H&E staining of tumor tissues showed that there were a large number of necrotic or apoptotic cells in the group with RmGIB NPs but no obvious cell death in the other groups, indicating that RmGIB NPs had a strong anti-tumor effect [36].

4. Conclusions

In summary, a nanocarrier with high loading capacity encapsulated by BSA was constructed, relying on RBCm *in vivo* for stability. GIB NPs were prepared by nab™ technology utilizing differences in solubility,

resulting in high loading capacities of 24.3 ± 1.2 % and 25.0 ± 1.2 %, respectively, for GA and ICG. RBCm as a natural cell membrane can be used to prolong the circulating time of nanoparticles *in vivo* to avoid clearance by the immune system, leading to a high accumulation rate in tumor tissue. This resulted in high efficiency and low toxicity for combination therapy *in vivo* and *in vitro*, respectively. In conclusion, RmGIB NPs are a potential platform for cancer treatment due to their high drug loading ability and unique biomimetic capability in avoiding immune clearance.

Credit author statement

Yuangang Liu and Shibin Wang conceptualized the project.

Pei Wang designed and performed nanoparticle synthesis, and *in vivo* experiments.

Fuquan Jiang contributed to the Hemolysis experiment and revision.

Biaoqi Chen and Hanxiao Tang performed electron microscopy experiments

Xiaojiao Zeng performed the release of drugs.

Duanhua Cai and Mingzhi Zhu performed the isolation of red blood cell membranes.

Ruimin Long and Dayun Yang performed the analysis.

Pei Wang, Fuquan Jiang, Shibin Wang, and Yuangang Liu acquired funding for this project.

Pei Wang, Ranjith Kumar Kankala, and Yuangang Liu designed visualizations of this submission. All authors contributed to the review and editing of the manuscript.

Declaration of Competing Interest

The authors have declared that there are no conflicts of interest in this work.

Acknowledgments

We are grateful for the assistance of National Marine Economic Innovation and Development Project (16PYY007SF17), the Science Research Foundation of National Health and Family Planning Commission of PRC & United Fujian Provincial Health and Education Project for Tacking the Key Research (WKJ2016-2-22), Program for Innovative Research Team in Science and Technology in Fujian Province University, Natural Science Foundation of Fujian Province of China (2015J05169), Subsidized Project for Postgraduates' Innovative Fund in Scientific Research of Huaqiao University, and Open Project of Key Laboratory of Cancer and Neurodegenerative Disease Transformation in Fujian Province (FMUCN-201801).

Appendix A. Supplementary data

Supplementary material related to this article can be found, in the online version, at doi:https://doi.org/10.1016/j.colsurfb.2020.110842.

References

[1] X. Hu, S. Zhai, G. Liu, D. Xing, H. Liang, S. Liu, Concurrent drug unplugging and permeabilization of polyprodrug-gated crosslinked vesicles for cancer combination chemotherapy, Adv. Mater. 30 (2018) 1706307–1706314.

[2] M. Zheng, C. Yue, Y. Ma, P. Gong, P. Zhao, C. Zheng, Z. Sheng, P. Zhang, Z. Wang, L. Cai, Single-step assembly of Dox/ICG loaded lipid-polymer nanoparticles for highly effective chemo-photothermal combination therapy, ACS Nano 7 (2013) 2056–2067.

[3] D. Lane, Designer combination therapy for cancer, Nat. Biotechnol. 24 (2006) 163–164.

[4] L. Hui, S. Qin, L. Yang, Upper critical solution temperature polymer, photothermal agent, and erythrocyte membrane coating: an unexplored recipe for making drug carriers with spatiotemporally controlled cargo release, ACS Biomater. Sci. Eng. 2 (2016) 2127–2132.

[5] Y. Yang, W. Zhu, Z. Dong, Y. Chao, L. Xu, M. Chen, Z. Liu, 1D coordination polymer nanofibers for low-temperature photothermal therapy, Adv. Mater. 29 (2017) 1703588–1703600.

[6] Y. Zhang, D. Yang, H. Chen, W. Lim, F. Phua, G. An, P. Yang, Y. Zhao, Reduction-sensitive fluorescence enhanced polymeric prodrug nanoparticles for combinational photothermal-chemotherapy, Biomaterials 163 (2018) 14–24.

[7] Y. Han, R.K. Kankala, S. Wang, A. Chen, Leveraging engineering of indocyanine green-encapsulated polymeric nanocomposites for biomedical applications, Nanomaterials 8 (2018) 360–387.

[8] J. Hu, Y. Cheng, X. Zhang, Recent advances in nanomaterials for enhanced photothermal therapy of tumors, Nanoscale 10 (2018) 22657–22672.

[9] Y. Liu, P. Bhattarai, Z. Dai, X. Chen, Photothermal therapy and photoacoustic imaging via nanotheranostics in fighting cancer, Chem. Soc. Rev. 48 (2018) 2053–2109.

[10] Y. Li, G. Liu, J. Ma, J. Lin, H. Lin, G. Su, D. Chen, S. Ye, X. Chen, X. Zhu, Z. Hou, Chemotherapeutic drug-photothermal agent co-self-assembling nanoparticles for near-infrared fluorescence and photoacoustic dual-modal imaging-guided chemo-photothermal synergistic therapy, J. Control. Release 258 (2017) 95–107.

[11] W. Tang, W. Tang, A. Szeitz, J. Kulkarni, P. Cullis, S. Li, Systemic study of solvent-assisted active loading of gambogic acid into liposomes and its formulation optimization for improved delivery, Biomaterials 166 (2018) 13–26.

[12] Y. Yang, Y. Liu, C. Cheng, H. Shi, H. Yang, H. Yuan, C. Ni, Rational design of GO-modified Fe3O4/SiO2 nanoparticles with combined rhenium-188 and gambogic acid for magnetic target therapy, ACS Appl. Mater. Interfaces 9 (2017) 28195–28208.

[13] R.K. Kankala, C. Liu, A. Chen, S. Wang, P. Xu, L. Mende, C. Liu, C. Lee, Y. Hu, Overcoming multidrug resistance through the synergistic effects of hierarchical pH-sensitive, ROS-generating nanoreactors, ACS Biomater. Sci. Eng. 3 (2017) 2431–2442.

[14] S. Rohiwal, A. Tiwari, G. Verma, S. Pawar, Preparation and evaluation of bovine serum albumin nanoparticles for ex vivo colloidal stability in biological media, Colloids Surf. A-Physicochem Eng. Asp. 480 (2015) 28–37.

[15] C. Javier, S. Cristina, Nanoparticle albumin-bound (nab™)-paclitaxel: improving efficacy and tolerability by targeted drug delivery in metastatic breast cancer, Eur. J. Cancer 8 (2010) 1–10.

[16] H. Chen, W. Zhang, G. Zhu, J. Xie, X. Chen, Rethinking cancer nanotheranostics, Nat. Rev. Mater. 2 (2017) 17024–17042.

[17] Q. Sun, Z. Zhou, N. iu, Y. Shen, Rational design of Cancer nanomedicine: nanoproperty integration and synchronization, Adv. Mater. 29 (2017) 1606628–1606646.

[18] A. Mikhail, C. Allen, Block copolymer micelles for delivery of cancer therapy: transport at the whole body, tissue and cellular levels, J. Control. Release 138 (2009) 214–223.

[19] S. Li, L. Huang, Pharmacokinetics and biodistribution of nanoparticles, Mol. Pharm. 5 (2008) 496–504.

[20] E. Blanco, H. Shen, M. Ferrari, Principles of nanoparticle design for overcoming biological barriers to drug delivery, Nat. Biotechnol. 33 (2015) 941–951.

[21] M. Ernsting, M. Murakami, A. Roy, S. Li, Factors controlling the pharmacokinetics, biodistribution and intratumoral penetration of nanoparticles, J. Control. Release 172 (2013) 782–794.

[22] A. Banerjee, J. Qi, R. Gogoi, J. Wong, S. Mitragotri, Role of nanoparticle size, shape and surface chemistry in oral drug delivery, J. Control. Release 238 (2016) 176–185.

[23] Y. Yang, D. Nie, Y. Liu, M. Yu, Y. Gan, Advances in particle shape engineering for improved drug delivery, Drug Discov. Today (2018) 1359–1368.

[24] K. Knop, R. Hoogenboom, D. Fischer, U. Schubert, Poly(ethylene glycol) in drug delivery: pros and cons as well as potential alternatives, Angew. Chem. Int. Ed. Engl. 49 (2010) 6288–6308.

[25] A. Kolate, D. Baradia, S. Patil, I. Vhora, G. Kore, A. Misra, PEG – a versatile conjugating ligand for drugs and drug delivery systems, J. Control. Release 192 (2014) 67–81.

[26] C. Hu, L. Zhang, S. Aryal, C. Cheung, R. Fang, L. Zhang, Erythrocyte membrane-camouflaged polymeric nanoparticles as a biomimetic delivery platform, Proc. Natl. Acad. Sci. U. S. A. 108 (2011) 10980–10985.

[27] J. Guo, P. Guan, W. Ding, S. Wang, X. Huang, Z. Wang, P. Wang, Erythrocyte membrane-encapsulated celecoxib improves the cognitive decline of Alzheimer's disease by concurrently inducing neurogenesis and reducing apoptosis in APP/PS1 transgenic mice, Biomaterials 145 (2017) 106–127.

[28] S. Thamphiwatana, P. Angsantikul, T. Escajadillo, Q. Zhang, J. Olson, B. Luk, S. Zhang, R. Fang, W. Gao, V. Nizet, L. Zhang, Macrophage-like nanoparticles concurrently absorbing endotoxins and proinflammatory cytokines for sepsis management, Proc. Natl. Acad. Sci. U. S. A. 114 (2017) 11488–11493.

[29] J. Li, X. Zhen, Y. Lyu, Y. Jiang, J. Huang, K. Pu, Cell membrane coated semiconducting polymer nanoparticles for enhanced multimodal cancer phototheranostics, ACS Nano 12 (2018) 8520–8530.

[30] C. Hu, R. Fang, K. Wang, B. Luk, S. Thamphiwatana, D. Dehaini, P. Nguyen, P. Angsantikul, C. Wen, A. Kroll, C. Carpenter, M. Ramesh, V. Qu, S. Patel, J. Zhu, W. Shi, F. Hofman, T. Chen, W. Gao, K. Zhang, S. Chien, L. Zhang, Nanoparticle biointerfacing by platelet membrane cloaking, Nature 526 (2015) 118–121.

[31] J. Copp, R. Fang, B. Luk, C. Hu, W. Gao, K. Zhang, L. Zhang, Clearance of pathological antibodies using biomimetic nanoparticles, Proc. Natl. Acad. Sci. U. S. A. 111 (2014) 13481–13486.

[32] Y. He, J. Qin, S. Wu, H. Yang, H. Wen, Y. Wang, Cancer cell-nanomaterial interface: role of geometry and surface charge of nanocomposites in the capture efficiency and cell viability, Biomater. Sci. (2019) 2759–2768.

[33] X. Lin, Y. Cao, J. Li, D. Zheng, S. Lan, Y. Xue, F. Yu, M. Wu, X. Zhu, Folic acid-modified Prussian blue/polydopamine nanoparticles as an MRI agent for use in

targeted chemo/photothermal therapy, Biomater. Sci. (2019) 2996–3006.
[34] M. Xuan, J. Shao, L. Dai, J. Li, Q. He, Macrophage cell membrane camouflaged Au nanoshells for in vivo prolonged circulation life and enhanced cancer photothermal therapy, ACS Appl. Mater. Interfaces 8 (2016) 9610–9618.
[35] M. Abbaci, A. Conversano, F. De Leeuw, C. Laplace-Builhe, C. Mazouni, Near-infrared fluorescence imaging for the prevention and management of breast cancer-related lymphedema: a systematic review, Eur. J. Surg. Oncol. (2019) 1–9.
[36] W. Chen, K. Zeng, H. Liu, Q. Jiang, L. Wang, Y. Liu, H. Wang, L. Deng, Y. Liu, Cell membrane camouflaged hollow prussian blue nanoparticles for synergistic photothermal-/chemotherapy of cancer, Adv. Funct. Mater. 27 (2017) 1605795.